

Simultaneous calorimetric and quick-EXAFS measurements to study the crystallization process in phase-change materials

Peter Zalden,^a Giuliana Aquilanti,^b Carmello Prestipino,^c Olivier Mathon,^d Bérangère André,^e Matthias Wuttig^{a,f} and Marie-Vanessa Coulet^{e*}

^aPhysikalisches Institut der RWTH, Lehrstuhl für Physik neuer Materialien, 52056 Aachen, Germany, ^bXAFS Beamline, Sincrotrone Trieste SCpA, SS 14 km 163.5, 34149 Basovizza, Trieste, Italy, ^cUMR CNRS 6226, Sciences Chimiques de Rennes, Campus de Beaulieu, Bâtiment 10B, 263 avenue du Général Leclerc, 35042 Rennes Cedex, France, ^dESRF, BP 220, 38042 Grenoble Cedex 9, France, ^eIM2NP, UMR 6242, CNRS and Aix-Marseille Université, Campus de Saint Jérôme, 13397 Marseille Cedex 20, France, and ^fJARA-FIT, RWTH Aachen University, 52056 Aachen, Germany. E-mail: vanessa.coulet@im2np.fr

A Calvet-type differential scanning calorimeter has been implemented on a synchrotron beamline devoted to X-ray absorption spectroscopy. As a case study, the complex crystallization process in amorphous Ge₁₅Sb₈₅ phase-change material is followed by simultaneous calorimetric and quick-EXAFS measurements. A first crystallization at 514(1) K is related to the crystallization of an Sb-rich phase accompanied by segregation of Ge atoms. Upon further heating, the as-formed amorphous Ge regions crystallize at 604(1) K. A quantitative analysis of the latent heat allows a Ge₁₁Sb₈₉ stoichiometry to be proposed for the first crystallized phase.

Keywords: phase-change materials; phase separation; crystallization; amorphous.

1. Introduction

It is often difficult to correlate measurements of the electronic or atomic structure with a well defined point in the phase diagram of the system under study. The best way to accomplish this is to perform so-called *in situ* experiments, where the sample is kept in the state of interest while acquiring the structural information. Such experiments rely on the assumption that during the measurements under specific thermodynamic conditions, such as temperature and pressure, the corresponding equilibrium structure given by the phase diagram will exist. The more complex the phase diagram of a system is, the more often this assumption is incorrect. The situation becomes even worse when kinetic effects govern the phase transitions and meta-stable phases are involved, since they are not even included in the phase diagram. This difficulty can be overcome when techniques to determine the atomic arrangement or electronic structure such as synchrotron-based techniques like diffraction or spectroscopy are simultaneously combined with differential scanning calorimetry (DSC). This technique allows identification of the response of the sample to an external stimulus which allows its exact thermodynamic state to be determined when measuring its structural and electronic properties.

The principle of coupling several techniques during a synchrotron experiment has progressed for more than 20 years. The combination of techniques includes light or Raman scattering with small- and wide-angle X-ray scattering (SAXS and WAXS) (Krüger & Zachmann, 1993; Bryant *et al.*, 1998), Fourier transform infrared spectroscopy (FTIR) with SAXS (Bras *et al.*, 1995) or with X-ray absorption spectroscopy (XAS) (Newton *et al.*, 2004), and even numerous combinations such as UV–vis, Raman and XAS (Briois *et al.*, 2005) or X-ray reflectivity, X-ray diffraction and sheet resistance measurements (Putero *et al.*, 2011). The coupling of DSC and X-ray techniques on synchrotron sources was first developed by Russell & Koberstein (1985). DSC, being a well established technique for monitoring the energetic changes during a phase transition, was combined with SAXS in order to study the melting and the crystallization in polymers. The instrumental set-up was further developed both by implementing other X-ray methods such as X-ray diffraction (Ungar & Feijoo, 1990; Yu & Liu, 1999) or XAS (Troger *et al.*, 1997) and by improving the calorimetric signal (Bras *et al.*, 1995; Keller *et al.*, 1998; Lexa, 2003; Ollivon *et al.*, 2006). So far, only soft condensed matter has been studied with this approach, utilizing phase transitions which occur at relatively low temperatures well below 500 K. In the present work we

propose to combine a calorimetric experiment with an extended X-ray absorption fine-structure spectroscopy (EXAFS) measurement in order to follow the crystallization process in phase-change materials (PCMs).

PCMs are defined by a remarkable combination of properties: (i) they exist in at least two (metastable) phases, (ii) the atomic re-arrangement between these two phases is very slow at room temperature (taking more than ten years) but can proceed extremely rapidly (10–100 ns) at elevated temperatures and (iii) the two phases possess large differences in their electrical or optical properties (Shportko *et al.*, 2008). Materials with such a property portfolio are ideally suited to store information both in optical and electrical data storage memories (Wuttig & Yamada, 2007). The recording of information is based on writing and erasing amorphous marks in a crystalline layer of a PCM (Wuttig & Yamada, 2007). In optical data storage media such as rewriteable CDs, DVDs and blu-ray discs, the writing process consists of heating the crystalline phase above its melting temperature and rapidly cooling so that it solidifies in the amorphous phase. The erasing process corresponds to the recrystallization of the amorphous mark. While the data retention is limited by the stability of amorphous marks at operating conditions, the speed of the device is limited by the re-crystallization process at elevated temperatures. Thus, the understanding of the atomic rearrangement and phase formation during the (re)-crystallization is of utmost importance in these systems. Being a core-level spectroscopy, XAFS can be applied to both non-crystalline and crystalline phases to follow the local environment of an element during the entire transformation process. By performing EXAFS data acquisition within 30 s (quick-EXAFS), the study of relatively fast phase transformations is facilitated.

In this work we present our set-up devoted to simultaneous DSC and quick-EXAFS measurements over a temperature range varying from room temperature up to 800 K. Contrary to the previous implementation of a DSC on a synchrotron beamline, we have employed a Calvet-type calorimeter (Höhne *et al.*, 2003) which consists of a heat-flux meter enabling precise measurements of the energy associated with the phase transitions. The combination of these two instruments is a non-trivial task since they request different requirements concerning the sample preparation. To achieve a good detection of the heat flux during a DSC measurement, the sample needs to be in good thermal contact with the measuring system. This requirement demands a large contact area between the sample and the heat sink of the calorimeter. For EXAFS measurements, however, the sample should be homogeneously distributed over all the incident X-rays and have a constant thickness. In addition, the absorption of X-rays by the sample could generate extra heat, which could affect the calorimetric signal. The following part of this paper will be thus devoted to the description of the experimental set-up and to the commissioning of the calorimeter in the coupling configuration. A detailed analysis of the crystallization process in $\text{Ge}_{15}\text{Sb}_{85}$ PCMs using simultaneous DSC/quick-EXAFS measurements will be presented in the third part.

2. Experimental set-up

2.1. Description of the calorimeter

Contrary to most equipment already used for coupling experiments (Bras *et al.*, 1995), the calorimetric measurements in this study were performed using a heat-flux differential scanning calorimeter with a cylinder-type system typically used in Calvet calorimeters (Höhne *et al.*, 2003). This calorimeter consists of a furnace enclosing two thin cylindrical tubes of alumina containing the reference and the sample (Sensys, SETARAM). Each tube is surrounded by several thermocouples commonly called thermopiles. The heat exchange between the tubes and the furnace is facilitated by these thermopiles which provide the dominant heat conduction paths and act as the temperature difference sensor. The primary signal is the temperature difference between the sample and the reference which is directly proportional to the heat flow rate. As will be discussed later, the use of such a DSC apparatus provides access to the enthalpy values associated with the phase transitions (Höhne *et al.*, 2003). To ensure good heat conduction, the tubes containing the sample and the reference must be exposed to gas flow. The standard gas inlet and outlet were modified in order to implement windows for the incoming and outgoing X-rays. Aluminized Mylar foils were chosen in order to minimize the radiation loss (see Fig. 1).

A calibration in temperature and in energy of the calorimeter is mandatory to obtain quantitative data from a DSC experiment and the procedure will be described later. First, the calibration factor depends on the sample location inside the tubes (see Fig. 1) and on the nature of the container. Both were kept unchanged during the experiment. Second, the calibration also depends on the carrier gas since it plays an important role in the heat conduction. In the present set-up, helium carrier gas was employed to optimize the heat exchange between sample and furnace and to minimize the absorption of the incident and transmitted X-rays.

2.2. Sample preparation

In standard calorimetric measurements, the signal-to-noise ratio is proportional to the amount of sample material.

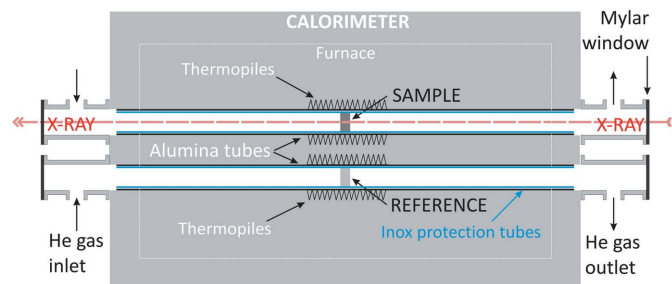


Figure 1 Experimental DSC/EXAFS set-up. The red double-headed arrow indicates the direction of the X-ray beam, which passes through the sample compartment of the DSC. Sample and reference consist mainly of pressed BN, which is admixed homogeneously with powder of the specimen (see text). The thermal conductivity and X-ray transmittivity are found to be sufficient to maintain calorimetric conditions and obtain EXAFS spectra simultaneously.

Generally the material is inside a special sample container which ensures the best thermal contact with the outer parts of the calorimeter. By combining calorimetry with EXAFS we had to accept a compromise by which the sample is mechanically fixed and distributed homogeneously over the beam cross section, but is still in an acceptable thermal contact to obtain a precise calorimetric signal. In addition, its thickness has to be chosen in a way to optimize the signal-to-noise ratio in the EXAFS spectra. Our solution to the challenges described above was to disperse the material in a boron nitride (BN) matrix and to press this mixture into a self-sustaining pellet. BN is an inert matrix material which has a better thermal stability than cellulose, since it melts only above 3000 K (Bundy & Wentorf, 1963). It is therefore expected that the temperature range of studies can be extended up to the technical limit of the calorimeter of 900 K.

The optimized mass of the sample for EXAFS measurements was then diluted into 100 mg of BN. The resulting pellets had a thickness of around 3 mm and could stand on their edge so that a sample container was no longer needed. As explained previously, the heat flow rate is proportional to the temperature difference between the sample and the reference, and hence it is important to choose a reference with similar heat capacity and thermal conductivity. Generally, when a container is used, the reference consists of a similar empty container having the same mass (*i.e.* the same thermal capacity) as that containing the sample. In the present case the reference consists of a pure BN pellet with the same thermal capacity as that containing the sample (*i.e.* with a mass around 100 mg). The EXAFS measurements necessitate this sample preparation, which reduces the thermal contact between the sample and the heating element as compared with the common containers, but nevertheless, owing to the sensitivity of the calorimeter type employed, high-quality thermodynamic data can still be obtained as shown below.

2.3. Commissioning of the DSC under the beam

The DSC was calibrated prior to the synchrotron experiment with exactly the same sample geometry and operating conditions (use of Mylar windows, inox protection tubes and He as carrier gas). The calibration of temperature and energy was performed using the melting of high-purity In, Sn, Pb and Sb samples prepared as ingots of 30 mg inside a 100 mg BN pellet. The heat-flow dependence of the calibration factor was taken into account by performing the measurements of the In and Sn references at 5 K min⁻¹ and 10 K min⁻¹ while the Pb and Sb pellet were only measured at 10 K min⁻¹. The calibration was performed using standard values as proposed by Stølen & Grønvold (1999).

In order to study the effect of the X-ray absorption on the calorimetric signal, the melting of the Sn reference was performed under the X-ray beam. The energy of the incident beam was fixed at 11.1 keV which ensures maximum absorption. The heating rate was 5 K min⁻¹ for the two measurements with and without the beam. As seen in Fig. 2, the DSC curves are very similar except for a slight variation in the

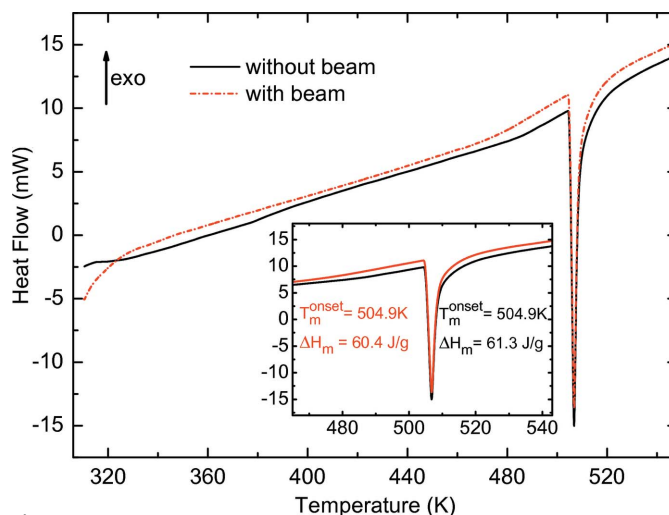


Figure 2

Calorimetric scan of the melting of a pure Sn reference sample with and without the X-ray beam, which was set to 11.1 keV, where the absorption by Sn is high. The small shift in the baseline might originate from the X-ray absorption or from a repositioning of the sample. The resulting temperatures and enthalpies are reliable in both cases, since they are unaffected by the X-rays and are in good agreement with literature values.

baseline, which could be related either to slight differences in the positioning of the sample and the reference or to absorption effects owing to the X-ray beam. Since it is not our aim to determine specific heats, this shift of the baseline is irrelevant for the experiments.

For each curve an endothermic peak is observed and can be assigned to the melting of the Sn reference. The melting temperature can be defined by the onset temperature T_m^{onset} extrapolated from the inflexion point and the area under this peak is directly related to the melting enthalpy ΔH_m (Höhne *et al.*, 2003). As seen on Fig. 2, the melting temperature and the enthalpy are not modified by the presence of the beam. The values for the melting temperature and the melting enthalpy are $T_m^{\text{onset}} = 504.9(1)$ K and $\Delta H_m = 60(1)$ J g⁻¹ with the beam, and $T_m^{\text{onset}} = 504.9(1)$ K and $\Delta H_m = 61(1)$ J g⁻¹ without it. Both numbers are in good agreement with standard values (505.1 K, 60.1 J g⁻¹) (Stølen & Grønvold, 1999). This suggests that the calibration procedure is correct.

3. Crystallization of amorphous Ge₁₅Sb₈₅

3.1. Scientific background

In recent years the majority of investigations of PCMs have focused on ternary alloys on the pseudo-binary line between GeTe and Sb₂Te₃ (Abrikosov & Danilova-Dobryakova, 1965), with special emphasis on Ge₂Sb₂Te₅ (Lencer *et al.*, 2011; Raoux & Wuttig, 2009). This particular compound has been proven to be suitable for both optical and electrical data storage (Yamada *et al.*, 1991), but does not switch very rapidly (Ozatay *et al.*, 2008) (*i.e.* no crystallization times shorter than 10 ns have been reported) and has a relatively low crystallization temperature, which is a disadvantage in high-temperature environments as encountered in automotive

applications. To eliminate these drawbacks, new PCMs have been developed such as $\text{Ge}_{15}\text{Sb}_{85}$ alloys with low Ge content. This particular compound was proven to crystallize at 514 K, and has a minimum crystallization time of just 400 ps at elevated temperatures (Siegel *et al.*, 1999). Moreover, it presents a low melting temperature which is also beneficial for application in memory devices since it contributes to decrease the power consumption during the switching.

The binary phase diagram of Ge–Sb is quite simple as it only contains a eutectic transformation located between 13 and 17 at% Ge and at 865 K (Chevalier, 1989). The phases involved are the liquid and the solid solutions of Ge in (Sb) as well as Sb in (Ge). For standard bulk sample preparations the mutual solid solubilities of the elements are low: the solid solubility of Ge in (Sb) is reported to be between 0 at% (Chevalier, 1989) and 2.5 at% Ge (Hansen, 1958), while (Ge) dissolves less than 0.02 at% Sb. However, it has been proposed by Giessen & Borromee-Gautier (1972) that a rapid quenching from the melt can enhance the solid solubility of Ge in (Sb) to more than 17 at%.

As mentioned above, $\text{Ge}_{15}\text{Sb}_{85}$ does not only possess a low melting temperature and short crystallization times at elevated temperatures (Siegel *et al.*, 1999; Afonso *et al.*, 1992), it also exhibits the required attributes in terms of pronounced changes of electrical resistivity (Krebs *et al.*, 2009) and optical reflectivity (Wiggins *et al.*, 2005) upon crystallization. However, a two-step crystallization process is consistently reported in several DSC measurements (Cabral *et al.*, 2008; Raoux *et al.*, 2009; Zalden *et al.*, 2010; Krusin-Elbaum *et al.*, 2010). Since reflections of Ge have been observed by X-ray diffraction after the second transition occurring around 604 K, it was concluded that a Ge phase was segregated. This tendency towards phase separation might impose new challenges for the application of $\text{Ge}_{15}\text{Sb}_{85}$ in memory technology, which relies on the reproducibility of the switching behavior. The two-step crystallization process has been interpreted differently by various authors: the first model assumes that crystalline Ge is segregated (or precipitated) during the second heat release (Cabral *et al.*, 2008; Raoux *et al.*, 2009; Krusin-Elbaum *et al.*, 2010); the second model is based on the segregation of amorphous Ge during the first heat release and the subsequent crystallization of this amorphous Ge, thus giving rise to the second heat release (Zalden *et al.*, 2010). Hence, this composition can be used as a model system for our coupled EXAFS and DSC experiments since it could be possible to follow simultaneously both the structural transitions and the heat release. This could reveal whether amorphous Ge is segregated during the first heat release or crystalline Ge is segregated during the second heat release.

3.2. Experimental details

X-ray absorption measurements were carried out at BM29 beamline at the ESRF (Grenoble, France) (De Panfilis *et al.*, 2000). The monochromator is a double-crystal fixed-exit double-cam-type from Kohzu-Seiki Corporation (Japan). A Si(311) crystal pair was employed to have an operational

energy range from 5 keV to 50 keV. The data collection was performed in transmission mode at the *K*-absorption edges of the two elements Ge (11.103 keV) and Sb (30.491 keV) to study changes of local order around each absorber. In order to follow the kinetics of the phase transition, the spectra were acquired in quick-EXAFS mode which was recently implemented on the BM29 beamline (Prestipino *et al.*, 2011). This method consists of a continuous scan of the angle of the monochromator during the acquisition (Frahm, 1989) allowing a drastic reduction of acquisition time with a signal-to-noise ratio comparable with the standard step-by-step mode. Acquisition times around 20 s per spectrum could be reached for the samples presented here. This fits well with the crystallization dynamics of $\text{Ge}_{15}\text{Sb}_{85}$ amorphous alloys at a heating rate of 5 K min^{-1} , where crystallization proceeds in 2 min (Zalden *et al.*, 2010).

Amorphous thin films of $\text{Ge}_{15}\text{Sb}_{85}$ with a thickness of $\sim 1\text{--}2 \mu\text{m}$ were deposited on silica substrates by magnetron sputtering from stoichiometric targets at the Department of Physics of RWTH Aachen, Germany. The experimental protocol followed during the sputtering was exactly the same as that described by Zalden *et al.* (2010). Considering the high reproducibility of the process, the samples are considered in the following as completely amorphous. The Rutherford backscattering spectroscopy measurements gave a stoichiometry of $\text{Ge}_{16(1)}\text{Sb}_{84(1)}$. The films were scraped from the substrate into powder using silica slides to avoid metallic contamination of the sample. The pellets were prepared by mixing together approximately 100 mg of BN and the necessary quantity of $\text{Ge}_{15}\text{Sb}_{85}$ to obtain an edge-step jump of around 1.5. This corresponds to $\sim 5 \text{ mg}$ at the Ge *K*-edge (11.1 keV) and $\sim 17 \text{ mg}$ at the Sb *K*-edge (33 keV). In the following the samples will be denoted as $(\text{Ge}_{15}\text{Sb}_{85})^{\text{Ge}}$ and $(\text{Ge}_{15}\text{Sb}_{85})^{\text{Sb}}$, respectively. The homogeneity of the powder was improved by using a vibrational ball milling and the pellets were prepared by applying a pressure of 2 bar.

3.3. Results

3.3.1. DSC results. Fig. 3 shows the DSC curves obtained for the two samples. In agreement with previous works (Cabral *et al.*, 2008; Raoux *et al.*, 2009; Zalden *et al.*, 2010; Krusin-Elbaum *et al.*, 2010) a two-step process is clearly observed as shown by the two endothermic peaks. However, owing to the very small amount of sample (5 mg at the Ge edge) imposed by the EXAFS conditions, the second crystallization peak is difficult to discern in the case of $(\text{Ge}_{15}\text{Sb}_{85})^{\text{Ge}}$. In the following the onset temperature and heat flux calculations were performed using the same temperature limits for the two samples. This is justified by the identical heating rate in both experiments. The integration limits were chosen using the $(\text{Ge}_{15}\text{Sb}_{85})^{\text{Sb}}$ sample where the signal is larger owing to the higher sample mass. The errors were calculated taking into account the errors both for the sample mass (5%) and the integration limits.

The onset temperatures and associated heat flux were determined as described in §2.3. As seen in Table 1, the values obtained are in good agreement with those published in the

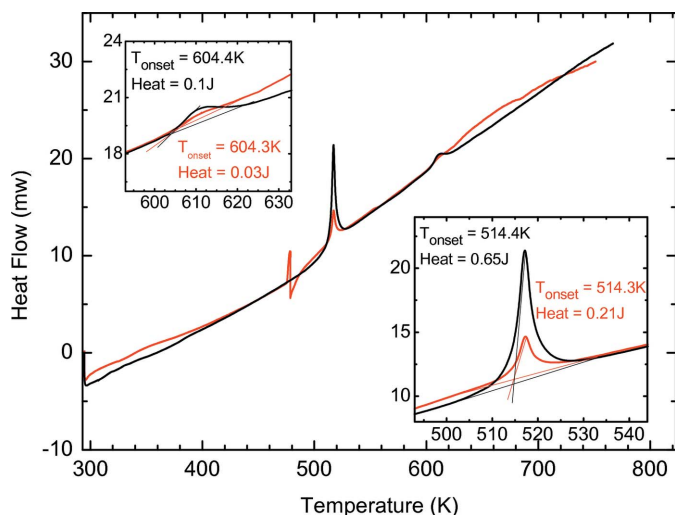


Figure 3 DSC temperature scan performed at 5 K min^{-1} for the $(\text{Ge}_{15}\text{Sb}_{85})^{\text{Sb}}$ (black) and for the $(\text{Ge}_{15}\text{Sb}_{85})^{\text{Ge}}$ (red) samples. A clear exothermic signal is observed at 514 K in both scans (right inset), followed by a second smaller exothermic signal. The first heat release originates from the crystallization of a Sb-rich phase and the segregation of amorphous Ge, whereas the second peak is a result of the crystallization of the amorphous Ge at 604 K (left inset). The glitch observed on the scan at the Ge edge is related to a pause of a few minutes during beam loss.

literature (Cabral *et al.*, 2008; Zalden *et al.*, 2010). The onset temperatures are the same at the two edges while the enthalpy slightly differs.

3.3.2. EXAFS results. The EXAFS oscillations $k^2\chi(k)$ at the Ge and Sb edge are presented in Fig. 4. To improve the clarity of presentation, only every tenth spectrum is plotted. The data presented have been obtained after pre-edge subtraction, edge-step normalization and fine-structure oscillation extraction using the software *Athena* (Ravel & Newville, 2005). The Fourier transformation was performed with a window function between 3 and 15 \AA^{-1} at the Sb edge and between 4 and 15 \AA^{-1} at the Ge edge. The background spline was adjusted to remove the background in real space up to 1.1 \AA for both edges. At the Ge *K*-edge, two clear changes are visible at temperatures around 510 K and 610 K. During the first transition, a significant change in the amplitude takes place accompanied by small changes in the frequency of the oscillations. This is indicative of a pronounced structural rearrangement of atoms around Ge. The second transition is basically an increase in amplitude, like that observed when a specific short-range order is becoming more pronounced. At the Sb *K*-edge the changes are more difficult to interpret since they mainly consist of a change in oscillation amplitude. The larger difference in EXAFS oscillations at the Ge edge as compared with the Sb edge shows that there is a stronger rearrangement of Ge bonds than Sb bonds.

3.3.3. Combined DSC–EXAFS analyses. The EXAFS analyses were carried out using the *ifffit* software (Newville, 2001) for every data set. The phase-separation tendency justifies an independent fitting of the two edges. At these measurement temperatures the useful signal for $\text{Ge}_{15}\text{Sb}_{85}$ is limited to the first coordination shell in all phases; more

Table 1

Experimental crystallization temperatures and corresponding enthalpies obtained from DSC measurements from a direct heating experiment of as-deposited amorphous $\text{Ge}_{15}\text{Sb}_{85}$ at 5 K min^{-1} ; the results compare well with those obtained from the literature.

	$T_{\text{cryst1}}^{\text{onset}}$ (K)	ΔH_{cryst1} (J g^{-1})	$T_{\text{cryst2}}^{\text{onset}}$ (K)	ΔH_{cryst2} (J g^{-1})
This work (Sb edge)	514(1)	37(3)	604(1)	6(1)
This work (Ge edge)	514(1)	40(3)	604(1)	6(1)
Zalden <i>et al.</i> (2010)	512	41(2)	606	7(2)
Cabral <i>et al.</i> (2008)	513	26	623	4

distant atoms only give a diffuse contribution. Therefore, the data were fitted after Fourier transformation, *i.e.* in *R*-space, where contributions from higher coordination shells can be filtered out more easily. The EXAFS data are treated by fitting scattering paths according to the common path expansion formalism. The scattering paths needed for this data treatment are the Ge–Ge and Ge–Sb paths for the data recorded at the Ge *K*-edge, and Sb–Ge and Sb–Sb paths for the data recorded

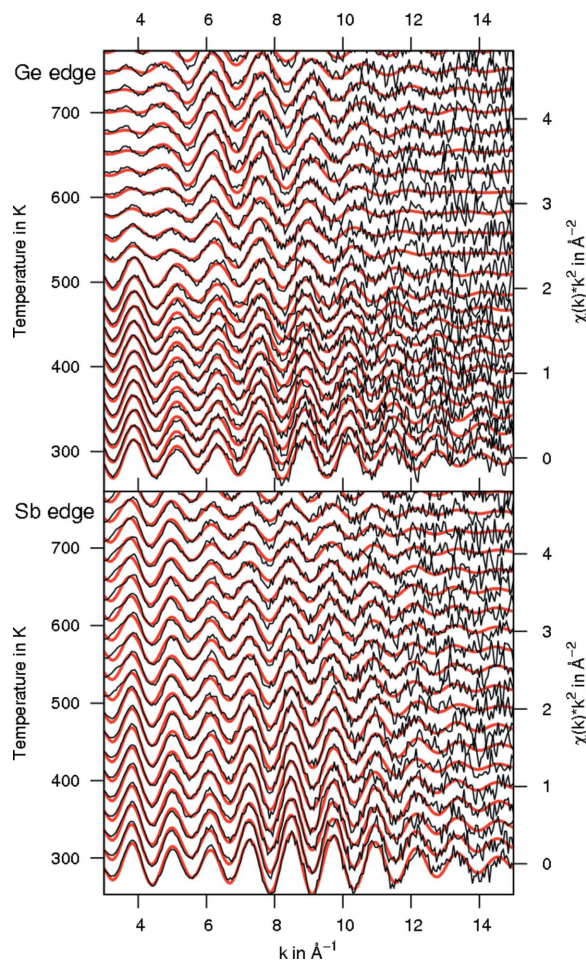


Figure 4 EXAFS oscillations at the Ge edge (top) and at the Sb edge (bottom). The extracted experimental data are plotted in black and the fits in red. Only every tenth spectrum is shown and the stacking increase of the data sets corresponds to the increase in measurement temperature. Transitions in the local atomic arrangement can be seen especially at the Ge edge around 510 K and 610 K, indicating that the local order around this element changes most significantly.

at the Sb *K*-edge. The necessary scattering functions for this path expansion least-squares fitting were extracted from several *Feff* calculations: the Sb–Sb scattering path was obtained from a rhombohedral (A7) crystal of Sb, the Ge–Sb and Sb–Ge paths from a crystal of Sb (A7) with some atoms replaced by Ge, and the Ge–Ge path was finally extracted from a calculation of pure crystalline Ge in the diamond (A4) structure.

At the Ge edge the fit was performed between 1.5 Å and 3.0 Å. As seen in Fig. 4, the performed fits in *R*-space allow $\chi(k)k^2$ curves (red line) to be calculated that are in very good agreement with the raw $\chi(k)k^2$ data (black line). Only one fitting model was used over the whole temperature range, which consists of one Ge–Sb and one Ge–Ge scattering path. The S_0^2 factor was set to 0.8 and the energy shift E_0 was set to 3.2 eV, and a single Debye–Waller factor was employed (Zalden *et al.*, 2010).

At the Sb edge the fitting range was increased up to 3.5 Å in *R*-space mainly because of the longer Sb–Sb bonds. Two different fitting models were used. The first model, from ambient temperature to 604 K, consists of one Sb–Sb scattering path and one Sb–Ge path. Although this model is perfectly suited to describe the initial as-deposited amorphous phase, the partial coordination number of Sb–Ge bonds decreases upon increasing the temperature above 517 K. This leads to larger error bars for the Sb–Ge distance, until finally, above 604 K, the contribution of Sb–Ge scattering paths is so small that no reliable information can be obtained. Therefore, the fitting model was modified by setting the Sb–Ge path to zero and including only Sb–Sb bonds above 604 K. The best test of this change is to check whether the remaining Sb–Sb parameters are changed by the imposed absence of Sb–Ge bonds. It is clear from Fig. 5 that there is no sudden change on the parameters for Sb–Sb bonds, so that this change is considered reliable. In both models S_0^2 was set to 0.83, the energy shift parameter E_0 was set to 7 eV (Zalden *et al.*, 2010) and a single Debye–Waller factor for each spectrum was used for the refinement over the whole temperature range. The other parameters were refined starting from the original bond lengths and coordination numbers in the crystalline structure for the Ge–Ge and Sb–Sb bonds. For Ge–Sb and Sb–Ge distances, the initial distance in the fitting procedure was 2.69 Å and a coordination number of 1 was guessed.

The results of the fit, *i.e.* the evolution of the distances and coordination numbers as a function of the temperature for both edges, are presented in Fig. 5, together with the corresponding calorimetric signal. Initially, each Ge

atom has on average 0.7 Ge atoms and 3.3 Sb atoms as nearest neighbors, which is consistent with the fourfold coordinated structure of amorphous Ge. At the Sb edge the number of Sb–Sb bonds dominates in the amorphous phase, simply owing to its large atomic fraction. Initially each Sb atom has on average 2.8 atoms of Sb as nearest neighbors and 0.8 atoms of Ge. The total coordination number of Sb in amorphous $\text{Ge}_{15}\text{Sb}_{85}$ is 3.6(3), which is larger than the value of 3.2(3) obtained during an earlier investigation based on low-temperature EXAFS data (Zalden *et al.*, 2010). The obtained value of 3.6(3) for the coordination number around Sb atoms, consistent with the connectivity of 4 reported by Hendus (1942) in amorphous Sb, could suggest that the 8-N rule is not fulfilled. However, the significant error bar of coordination numbers obtained from EXAFS analysis makes it impossible to clearly state whether the 8-N rule is applicable to amorphous $\text{Ge}_{15}\text{Sb}_{85}$.

When the first crystallization takes place at 514 K, clear changes occur at both edges. At the Ge edge the number of Sb neighbors strongly decreases from 3.3(2) down to 2.0(2) while the average number of Ge neighbors increases up to 2.0(2). Thus, during the first heat release, a change in bond connectivity takes place, switching from Sb to Ge as the most dominant bonding partner of Ge. At the same time, the Ge–Sb and Ge–Ge distances are not affected by the crystallization supporting the model of a change in connectivity only. At the Sb edge the number of heteropolar bonds, *i.e.* the number of Ge neighbors, decreases from 0.7(1) to 0.3(1), as expected from the investigation of the Ge edge. At the same time, the number of homopolar Sb–Sb bonds also decreases. This is

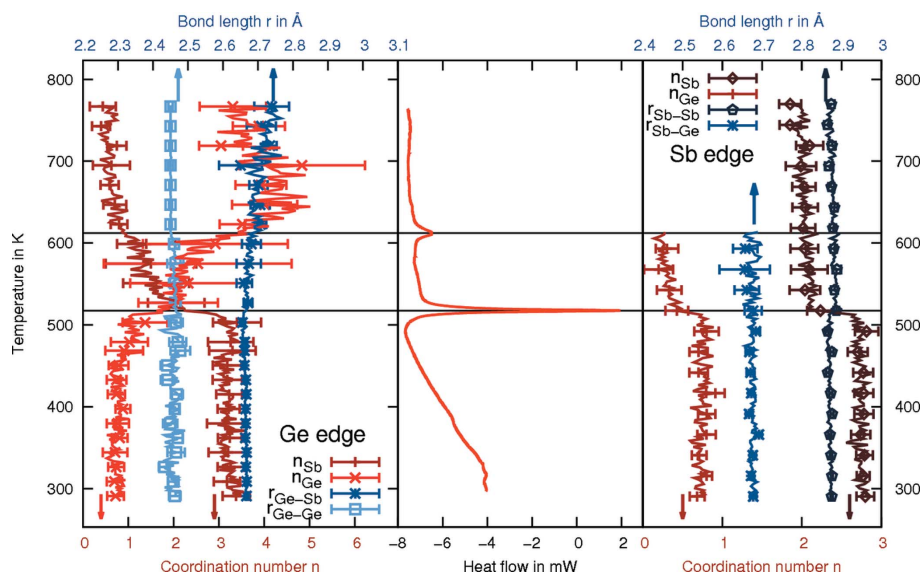


Figure 5

Temperature dependence of the distances and coordination numbers at the Ge edge (left) and at the Sb edge (right) together with the calorimetric signal measured for the $(\text{Ge}_{15}\text{Sb}_{85})_{\text{Sb}}$ sample (center). Note that for better legibility only every tenth point is shown with an error bar. At the first exothermic transition an exchange of bonds can be observed at the Ge edge: the number of Ge–Sb bonds is reduced while the number of Ge–Ge bonds increases. This trend is compatible only with a phase separation. This transition continues upon further heating the sample, until the second transition where the Ge–Ge bond length is reduced to that of crystalline Ge in the diamond structure (A4). This behavior shows that amorphous Ge is segregated at the first transition, and subsequently crystallizes at higher temperatures.

probably related to the decrease of coordination numbers upon crystallization in pure Sb (Hendus, 1942), decreasing from 4 in the amorphous to 3 in the crystalline phase.

After this first crystallization, the surrounding of Ge becomes more and more enriched by Ge upon substitution of Sb atoms. This is indicative of the formation of Ge-rich regions. At 604 K the calorimetric signal shows a second exothermic peak characteristic of a second crystallization. Since we cannot see any effect of this transition on the Sb–Sb coordination, this suggests that pure Ge regions, formed during and after the first transition, crystallize. After the second crystallization we find four Ge atoms in the nearest neighborhood of the absorbing Ge atom which is consistent with the structure of crystalline Ge.

The Debye–Waller factors of amorphous $\text{Ge}_{15}\text{Sb}_{85}$ (not shown here) were also determined by the fitting procedure. At both edges they both increase linearly until the crystallization occurs. At 514 K the temperature dependence then differs at the two edges: at the Ge edge the Debye–Waller factor retains its value from the amorphous phase and does not change significantly with temperature [around $\sigma_{\text{Ge}}^2 = 0.008(1) \text{ \AA}^2$]. At the Sb edge, however, the Debye–Waller factor suddenly decreases upon crystallization from $\sigma_{\text{Sb}}^2 = 0.009(1) \text{ \AA}^2$ to $\sigma_{\text{Sb}}^2 = 0.007(1) \text{ \AA}^2$ which is consistent with the onset of long-range order upon crystallization. Upon further heating, the Debye–Waller factor follows an expected linear and slight increase.

Assuming that the second crystallization peak is only due to the crystallization of Ge, it is possible to extract from the DSC data the quantity of Ge and the stoichiometry of the phase which first crystallizes. Dividing the observed enthalpy of 0.10(1) J by the value proposed by Turnbull (1982) for the enthalpy of crystallization of amorphous germanium ($\Delta H_{\text{cryst}}^{\text{Ge}} = 155 \pm 13 \text{ J g}^{-1}$), the crystallizing mass of Ge turns out to be equal to 0.6(1) mg. Considering that the total mass of Ge in $\text{Ge}_{15}\text{Sb}_{85}$ is 1.8(1) mg, we notice that less than one-third of the Ge atoms are involved in the second crystallization. The remaining Ge atoms either remain amorphous or are in solid solution with the Sb, which crystallized during the first heat release. Assuming that no Ge remains amorphous, the stoichiometry of the Sb-rich phase that has first crystallized can be estimated to be $\text{Ge}_{11(1)}\text{Sb}_{89(1)}$. This is in rather good agreement with the stoichiometry proposed by Zalden *et al.* (2010) using RMC where $\text{Ge}_{10}\text{Sb}_{90}$ and segregated amorphous Ge were found directly after the first crystallization.

The large number of EXAFS spectra taken during this experiment enables us to follow the temperature dependence of bond lengths. On average, the Ge–Ge and Sb–Sb bond lengths are in good agreement with literature values (Dalba *et al.*, 1995; Ichikawa, 1970). Interestingly, some interatomic distances show significant changes with temperature. Among these, we can distinguish continuous effects from sudden changes related to phase transitions. Continuous changes are visible for example for the Ge–Sb distances at the Ge edge below 514 K and for the Sb–Sb distances at the Sb edge above 514 K, which both slightly decrease with increasing temperature. Both structural relaxation and thermal expansion contribute to these changes and, since we cannot decouple

both effects based on the present data, we cannot quantify these effects. Statistically significant sudden changes are observed at 514 K at the Ge edge, where the Ge–Sb distances slightly increase, while simultaneously the Sb–Sb bond length at the Sb edge increases. The Sb–Sb distance in as-deposited amorphous $\text{Ge}_{15}\text{Sb}_{85}$ is 2.87(1) Å and increases up to 2.89(1) Å at the first crystallization. This increase is rather surprising but one can speculate that it is due to the additional influence of longer Sb–Sb bonds in crystalline Sb (Ichikawa, 1970).

4. Conclusion

Simultaneous DSC and quick-EXAFS experiments were performed to understand the crystallization process in $\text{Ge}_{15}\text{Sb}_{85}$ amorphous phase-change material. The combined analysis of these measurements shows that two crystallization events take place. The first one is linked to the crystallization of a rich Sb-phase and is accompanied by segregation of amorphous Ge. Upon further heating, the crystallization of the as-formed amorphous Ge-rich regions was shown based on its heat release in the calorimetric signal. The slight reduction of the Ge–Ge bond length in the EXAFS analysis further supports this result. The crystalline phase of $\text{Ge}_{15}\text{Sb}_{85}$ therefore consists of Sb-rich crystals with a maximum of 10 at% Ge and domains of amorphous or crystalline Ge, depending on the annealing temperature. For phase-change application the fact that the segregation occurs immediately after the crystallization of the Sb-rich phase (at 514 K) could be dramatic for device reliability since the chemical composition cannot be guaranteed. Finally, it was further shown that the coupling of DSC and quick-EXAFS is a valuable option for samples, where the calorimetric signal alone is not sufficient to identify phase transitions. The linear geometry of an EXAFS experiment in transmission mode together with the tube geometry of the DSC allows both techniques to be efficiently combined at a synchrotron beamline in order to investigate the atomic rearrangement upon well defined structural phase transitions. The present set-up is applicable when the following two requirements are fulfilled: the energy associated with the phase transition must be higher than 10 mJ and the amount of sample in the beam should be well chosen to optimize the signal-to-noise ratio of the EXAFS measurements.

Pierre Benigni and Jacques Rogez (IM2NP, Marseille) are acknowledged for valuable discussions and helpful advice concerning the modification of the calorimeter. Nathalie Nardone (SETARAM, France) is strongly acknowledged for her technical help during all the implementation procedures of the calorimeter. We acknowledge ESRF for providing beam time under project numbers MI980 and HS980, as well as Sebastien Pasternak and Antonia Beteva for their technical help on the BM29 beamline. This project between French and German teams was supported by the PHC-PROCOPE 2010 project numbers 25157ZB (French side) and 50749076

(German side). Some of the authors (MW and PZ) would like to acknowledge funding by the Deutsche Forschungsgemeinschaft (DFG) via SFB 917.

References

- Abrikosov, N. K. & Danilova-Dobryakova, G. T. (1965). *Izv. Akad. Nauk. SSSR Neorg. Mater.* **1**, 204–207.
- Afonso, C., Solis, J., Catalina, F. & Kalpouzos, C. (1992). *Appl. Phys. Lett.* **60**, 3123–3125.
- Bras, W., Derbyshire, G. E., Bogg, D., Cooke, J., Elwell, M. J., Komanschek, B. U., Naylor, S. & Ryan, A. J. (1995). *Science*, **267**, 996–999.
- Briois, V., Lützenkirchen-Hecht, D., Villain, F., Fonda, E., Belin, S., Griesebock, B. & Frahm, R. (2005). *J. Phys. Chem. A*, **109**, 320–329.
- Bryant, G., Gleeson, H., Ryan, A., Fairclough, J., Bogg, D., Goossens, J. & Bras, W. (1998). *Rev. Sci. Instrum.* **69**, 2114–2117.
- Bundy, F. P. & Wentorf, R. H. (1963). *J. Chem. Phys.* **38**, 1144–1149.
- Cabral, C. Jr, Krusin-Elbaum, L., Bruley, J., Raoux, S., Deline, V., Madan, A. & Pinto, T. (2008). *Appl. Phys. Lett.* **93**, 071906.
- Chevalier, P. Y. (1989). *Thermochim. Acta*, **155**, 227–240.
- Dalba, G., Fornasini, P., Grazioli, M. & Rocca, F. (1995). *Phys. Rev. B*, **52**, 11034–11043.
- De Panfilis, S., Ansell, S., Bowron, D., Filipponi, A., Borowski, M., Di Cicco, A. & Itie, J. (2000). *Rev. Sci. Instrum.* **71**, 2422–2432.
- Frahm, R. (1989). *Rev. Sci. Instrum.* **60**, 2515–2518.
- Giessen, B. C. & Borromee-Gautier, C. (1972). *J. Solid State Chem.* **452**, 447–452.
- Hansen, M. (1958). *Constitution of Binary Alloys*, 2nd ed. New York: McGraw-Hill.
- Hendus, H. (1942). *Z. Phys. A*, **119**, 265–286.
- Höhne, G., Hemminger, W. & Flammersheim, H.-J. (2003). *Differential Scanning Calorimetry*. Berlin/Hedeilberg/New York: Springer-Verlag.
- Ichikawa, T. (1970). *Jpn. J. Appl. Phys.* **9**, 748–760.
- Keller, G., Lavigne, F., Forte, L., Andrieux, K., Dahim, M., Loisel, C., Ollivon, M., Bourgaux, C. & Lesieur, P. (1998). *J. Therm. Anal.* **51**, 783–791.
- Krebs, D., Raoux, S., Rettner, C. T., Burr, G. W., Shelby, R. M., Salinga, M., Jefferson, C. M., Wuttig, M. & IBM/Macronix PCRAM Joint Project (2009). *J. Appl. Phys.* **106**, 054308.
- Krüger, K. & Zachmann, H. (1993). *Macromolecules*, **26**, 5202–5208.
- Krusin-Elbaum, L., Shakhvorostov, D., Cabral, C., Raoux, S. & Jordan-Sweet, J. L. (2010). *Appl. Phys. Lett.* **96**, 121906.
- Lencer, D., Salinga, M. & Wuttig, M. (2011). *Adv. Mater.* **23**, 2030–2058.
- Lexa, D. (2003). *Thermochim. Acta*, **398**, 241–248.
- Newton, M., Jyoti, B., Dent, A., Fiddy, S. & Evans, J. (2004). *Chem. Commun.* **21**, 2382–2383.
- Newville, M. (2001). *J. Synchrotron Rad.* **8**, 96–100.
- Ollivon, M., Keller, G., Bourgaux, C., Kalnin, D., Villeneuve, P. & Lesieur, P. (2006). *J. Therm. Anal. Calorim.* **85**, 219–224.
- Ozatay, O., Stipe, B., Katine, J. & Terris, B. D. (2008). *J. Appl. Phys.* **104**, 084507.
- Prestipino, C., Mathon, O., Hino, R., Beteva, A. & Pascarelli, S. (2011). *J. Synchrotron Rad.* **18**, 176–182.
- Putero, M., Ouled-Khachroum, T., Coulet, M.-V., Deleruyelle, D., Ziegler, E. & Muller, C. (2011). *J. Appl. Cryst.* **44**, 858–864.
- Raoux, S., Cabral, C., Krusin-Elbaum, L., Jordan-Sweet, J. L., Virwani, K., Hitzbleck, M., Salinga, M., Madan, A. & Pinto, T. L. (2009). *J. Appl. Phys.* **105**, 064918.
- Raoux, S. & Wuttig, M. (2009). Editors. *Phase Change Materials: Science and Applications*. New York: Springer-Verlag.
- Ravel, B. & Newville, M. (2005). *J. Synchrotron Rad.* **12**, 537–541.
- Russell, T. P. & Koberstein, J. T. (1985). *J. Polym. Sci.* **23**, 1109–1115.
- Shportko, K., Kremers, S., Woda, M., Lencer, D., Robertson, J. & Wuttig, M. (2008). *Nat. Mater.* **7**, 653–658.
- Siegel, J., Afonso, C. N. & Solis, J. (1999). *Appl. Phys. Lett.* **75**, 3102–3104.
- Stølen, S. & Grønvald, F. (1999). *Thermochim. Acta*, **327**, 1–32.
- Troger, L., Hilbrandt, N. & Epple, M. (1997). *Synchrotron Radiat. News*, **10**, 11–17.
- Turnbull, D. (1982). *J. Phys. Colloq.* **43**, C1-259–C1-269.
- Ungar, G. & Feijoo, J. (1990). *Mol. Cryst. Liq. Cryst.* **180**, 281–291.
- Wiggins, S. M., Bonse, J., Solis, J., Afonso, C. N., Sokolowski-Tinten, K., Temnov, V. V., Zhou, P. & von der Linde, D. (2005). *J. Appl. Phys.* **98**, 113518.
- Wuttig, M. & Yamada, N. (2007). *Nat. Mater.* **6**, 824–832.
- Yamada, N., Ohno, E., Nishiuchi, K., Akahira, N. & Takao, M. (1991). *J. Appl. Phys.* **69**, 2849–2856.
- Yu, Z. & Liu, Y. (1999). *J. Therm. Anal. Calorim.* **58**, 363–368.
- Zalden, P., Bichara, C., van Eijk, J., Braun, C., Bensch, W. & Wuttig, M. (2010). *J. Appl. Phys.* **107**, 104312.